



RESEARCH ARTICLE

10.1002/2015JD023739

Key Points:

- PW1-DW1 interaction is an important source of DW2
- The interaction couples the winter and the summer hemispheres
- The interaction transmits PW1 influences to at least 90 km

Correspondence to:

R. S. Lieberman,
r.s.lieberman@gats-inc.com

Citation:

Lieberman, R. S., D. M. Riggan, D. A. Ortland, J. Oberheide, and D. E. Siskind (2015), Global observations and modeling of nonmigrating diurnal tides generated by tide-planetary wave interactions, *J. Geophys. Res. Atmos.*, 120, 11,419–11,437, doi:10.1002/2015JD023739.

Received 1 JUN 2015

Accepted 26 OCT 2015

Accepted article online 28 OCT 2015

Published online 18 NOV 2015

Global observations and modeling of nonmigrating diurnal tides generated by tide-planetary wave interactions

R. S. Lieberman¹, D. M. Riggan¹, D. A. Ortland², J. Oberheide³, and D. E. Siskind⁴

¹GATS Inc., Boulder, Colorado, USA, ²Northwest Research Associates, Boulder, Colorado, USA, ³Department of Physics, Clemson University, Clemson, South Carolina, USA, ⁴Space Science Division, Naval Research Laboratory, Washington, District of Columbia, USA

Abstract Advective processes that couple planetary waves with tides have long been proposed as sources of nonmigrating diurnal tides. This paper reports observations of short-term variability in global observations of nonmigrating tides predicted to arise from the interaction of the migrating diurnal tide (DW1) with a quasi-stationary planetary wave number one (PW1). PW1 and tidal definitions are extracted from satellite temperatures and high-altitude meteorological analyses. During winter months, the evolution of westward traveling diurnal tides with zonal wave number 2 (DW2) generally tracks that of strong-amplitude stratospheric PW1. DW1 and PW1 spectra are used to compute nonlinear tidal forcing terms arising from advection. We then examine the response of a primitive equation model to the observation-based nonlinear forcing. The model experiments indicate that meridional advection of PW1 zonal momentum by DW1 is a significant source of lower thermospheric DW2. Modeled DW2 amplitudes are very consistent with observed DW2 amplitudes when stratospheric PW1 penetrates to equatorial latitudes. The model experiments also indicate that the interaction can imprint short-term variability associated with wintertime PW1 upon DW2 in the summer hemisphere and the lower thermosphere.

1. Introduction

Nonmigrating diurnal tides are a leading cause of longitudinal and temporal variability in middle atmosphere tides [Khattatov *et al.*, 1996; Hagan *et al.*, 1997; Miyahara *et al.*, 1999; Hagan and Forbes, 2002]. These components travel with an angular phase speed that differs from the angular frequency of Earth's rotation, or Ω . Examples are eastward propagating, zonally uniform, and westward traveling diurnal tides with zonal wave numbers other than one. A well-known source of terrestrial nonmigrating tides is the interaction of the diurnal harmonic of solar illumination with longitudinally nonuniform radiative and/or convective sources [Chapman and Lindzen, 1970; Sakazaki *et al.*, 2015]. A zonally uniform heating medium gives rise to a diurnal, westward traveling zonal wave number one (DW1) response that is Sun-synchronous or *migrating*. However, longitudinally varying heating agents produce higher-order zonal harmonics that do not follow the Sun. For example, latent heat release due to deep convection has been identified as a leading source of planetary-scale nonmigrating diurnal tides in the middle atmosphere [Hamilton, 1981; Forbes *et al.*, 1997a, 1997b; Hagan *et al.*, 1997; Hagan and Forbes, 2002].

Advective processes that couple planetary waves (PWs) with tides have long been proposed as sources of higher-order zonal and temporal harmonics in the middle atmosphere [Teitelbaum and Vial, 1991; Hagan and Roble, 2001; Angelats i Coll and Forbes, 2002]. The interaction of a tide with a planetary wave (PW) yields "secondary" waves with zonal wave numbers and frequencies given by the sums and the differences of the corresponding "parent" wave numbers and frequencies. Kuroda and Chiba [1995] found that the diurnally varying zonally symmetric (or $m=0$) tide in a general circulation model amplified as a result of interaction between DW1 and a stationary PW zonal wave number one (PW1). Palo *et al.* [1999] presented evidence for coupling between diurnal tides and the 2 day wave in the National Center for Atmospheric Research thermosphere-ionosphere-mesosphere-electrodynamics general circulation model (TIME-GCM). Hagan and Roble [2001] detected nonmigrating diurnal tides in TIME-GCM that had no apparent source other than the interaction of stationary PWs with DW1. Angelats i Coll and Forbes [2002] used a mechanistic, nonlinear spectral model to explore similar interactions between stationary PWs and the migrating semidiurnal tide.

©2015. The Authors.

This is an open access article under the terms of the Creative Commons Attribution-NonCommercial-NoDerivs License, which permits use and distribution in any medium, provided the original work is properly cited, the use is non-commercial and no modifications or adaptations are made.

Observational evidence for tide-PW connections comes largely from individual ground sites and is mostly associated with the semidiurnal tide. Measurements at the South Pole have revealed semidiurnal oscillations with a zonal wave number of one [Hernandez *et al.*, 1993; Forbes *et al.*, 1995], predicted to arise from the interaction between the migrating semidiurnal tide and PW1 [Angelats *i Coll and Forbes*, 2002]. Pancheva *et al.* [2002] inferred the zonal wave number structure of nonlinearly generated wave products from coordinated, multiple-site radar wind measurements. These findings were interpreted as further evidence of semidiurnal tide and PW interaction. Interactions between semidiurnal tides and transient waves are thought to cause modulations of semidiurnal winds on timescales associated with transient PWs [Manson and Meek, 1990; Canziani, 1994a; Hall *et al.*, 1995; Mitchell *et al.*, 1996; Kamalabadi *et al.*, 1997].

Owing to the global nature of semidiurnal tides, an important consequence of their interaction with PWs is the direct coupling of the summer and winter hemispheres. Quasi-stationary waves can attain large amplitudes but are confined to the winter stratosphere, whereas nonmigrating tides are present in both hemispheres. For example, Smith *et al.* [2007] examined semidiurnal variability at a single site (Esrang, 48°N, 21°E) and speculated that the cause was superposition of nonmigrating components that may have no local sources, reflecting instead the PW activity in the opposite hemisphere. Tide-PW interaction is also thought to facilitate coupling of the winter stratosphere to the low-latitude ionosphere. Forbes *et al.* [2008] suggested that winds associated with nonmigrating tides in the 100–170 km region induce longitudinal variability in the electric fields produced through the ionospheric dynamo mechanism, leading to modulation of vertical equatorial plasma drifts. A number of studies do in fact indicate connections between sudden stratospheric warming events and the ionosphere [Chau *et al.*, 2009, 2010; Goncharenko *et al.*, 2010].

Observational support for diurnal tide and PW interaction is more sparse. Canziani [1994a, 1994b] detected variations in thermospheric diurnal wind amplitudes with periods between 2 and 60 days and proposed nonlinear interactions with transient PWs as a possible source. Oberheide *et al.* [2002] and Oberheide and Gusev [2002] reported nonmigrating diurnal tides with zonal wave numbers zero (DS0) and two (DW2) in Cryogenic Infrared Spectrometers and Telescopes for the Atmosphere (CRISTA) measurements. These components are predicted by the interaction between DW1 and PW1. Lieberman *et al.* [2004] reported amplification of the same diurnal harmonics in Limb Infrared Monitor of the Atmosphere temperatures during November 1978 to January 1979, when PW1 was large and variable in the Northern Hemisphere.

While Oberheide *et al.* [2002] and Lieberman *et al.* [2004] provided some intriguing observational support for diurnal tide-PW interaction, their studies were limited in important ways. The brevity of the CRISTA mission resulted in the availability of only 2 days of data for tidal analysis by Oberheide *et al.* [2002]. This small sample precluded comparisons of middle atmosphere nonmigrating tide responses in the presence and the absence of PWs. The data set analyzed by Lieberman *et al.* [2004] had a longer time span (8 months), but extended only to 80 km, well below the levels where nonmigrating tides attain their largest amplitudes.

A more comprehensive understanding of tide-PW interactions clearly requires the use of extended time series from global satellite observations such as the Thermosphere-Ionosphere-Mesosphere Energetics and Dynamics (TIMED) and Earth Observing System (EOS). The most comprehensive tidal diagnostics to date are from the Sounding of the Atmosphere using Broadband Emission Radiometry (SABER) and TIMED Doppler interferometer [Zhang *et al.*, 2006; Oberheide *et al.*, 2006; Wu *et al.*, 2008a, 2008b]. However, these studies are based on space-time spectral analysis and rely on full (24 h) local solar time coverage. This inherently limits the time resolution because 60 days of TIMED data need to be averaged, due to the orbit geometry. The 60 day mean tidal quantities are insufficient for studying short-term tidal variability that characterizes tides generated through interactions with PWs.

This paper reports observations of short-term variability in DW2 and DS0 and presents evidence for DW1-PW1 interaction as a source of DW2. Our approach consists of extracting short-term definitions of PWs and diurnal tides from satellite data and meteorological analyses. These data and the analysis procedures are described in section 2. The behavior of DW2 in relation to stratospheric PW1 over several winter seasons is described in section 3. PW1 and DW1 diagnostics are used to compute nonlinear forcing terms arising from advection. We then examine the response of a primitive equation model to the observation-driven nonlinear forcing. These experiments are reported in section 4. Our results confirm that PW1-DW1 interaction is a significant source of DW2 during wintertime months when PW1 penetrates to equatorial latitudes. Our work also highlights the roles of DW2 for vertical and cross-hemispheric coupling.

2. Data

Our data analysis strategy consists of first identifying short-term diurnal tides in SABER temperatures and then verifying these with tidal proxies in concurrent EOS Aura Microwave Limb Sounder (MLS) temperatures. In order to explore quantitatively the relationships between DW1, PW1, and DW2, we require horizontal winds. These are obtained from a high-altitude forecast model (described in section 2.3) that assimilates middle atmosphere satellite temperatures.

2.1. SABER

SABER is a 10-channel infrared (1.27 to 16.9 μm) limb radiometer aboard TIMED that measures radiatively active species. Retrievals of temperature are obtained from infrared emissions of CO₂ at both 15 and 4.3 μm , from cloud tops to about 120 km. The vertical resolution is about 2 km. This study used Version 1.07 temperatures that were validated by Remsberg *et al.* [2008] against airglow- and sodium lidar-based temperatures in the mesosphere and lower thermosphere (MLT). Temperature precision in the MLT is about 5 K at 95 km. V1.07 retrievals span January 2002 to the present time; these are archived at http://saber.gats-inc.com/data_services.php.

Over the course of one TIMED orbit, SABER observes between 52°S and 83°N during the northward looking mode, switching after 60 days to an analogous southward viewing mode. On an individual day, SABER makes measurements covering 15 longitude bands. Daytime and nighttime measurements are nearly fixed with respect to local time, drifting backward by about 12 min on subsequent days. The difference between ascending and descending node local times at the equator ranges from approximately 8.5 to 9.3 h at equatorial latitudes, depending on whether SABER was in a northward viewing or southward viewing yaw period.

SABER samples 24 h of local time over a 60 day yaw period [Zhu *et al.*, 2005]. This is too lengthy of an averaging interval for study of tidal evolution during periods of rapid PW amplification. Short-term variations in tides can be inferred from differences between ascending and descending measurements nearly 12 h apart, which can be thought of as a global "snapshot" of the diurnal tide [Wallace and Hartranft, 1969; Wallace and Tadd, 1974; Hitchman and Leovy, 1985; Ward *et al.*, 1999]. Lieberman [1991] and Oberheide *et al.* [2000] demonstrated that amplitude and phase of DW1 can readily be estimated from the vertical structure of the zonal mean component of the ascending-descending difference pattern. However, the recovery of nonmigrating tides is more complex. A diurnal tide with a zonal wave number m is viewed by the satellite as a stationary zonal wave number k_s with a value of $m - 1$ in the case of westward propagation, and $k_s = m + 1$ if eastward propagating. Thus, an integer-valued k_s in SABER's ascending-descending node temperature spectrum represents the juxtaposition of a westward propagating diurnal tide with $m = k_s + 1$ and an eastward propagating diurnal tide with $m = k_s - 1$. (Note that DW1 is aliased to the zonal mean from the satellite perspective, or $k_s = 0$.)

Oberheide *et al.* [2002] developed a strategy for deconvolving the interference among satellite-viewed diurnal proxies. This method exploits the vertical structure of the zonal wave number m ascending-descending node difference pattern, hereafter referred to as T_m . At any given latitude and altitude, T_m is cast as a linear combination of an eastward traveling diurnal component with amplitude T_{m-1} and phase ϕ_{m-1} , and a westward traveling component with amplitude T_{m+1} and phase ϕ_{m+1} , that have been evaluated at the ascending and descending node local times and differenced. As shown by Oberheide *et al.* [2002], exact solutions of T_{m-1} , ϕ_{m-1} , T_{m+1} , and ϕ_{m+1} can be determined at the levels of the extrema of the T_m^2 curve, and at the midpoints between these extrema. Linear interpolation is then used to build the solutions at the remaining levels. A full description of the "deconvolution" methodology, including examples, is provided in Oberheide *et al.* [2002] and Lieberman *et al.* [2004].

The uncertainty of the amplitude retrievals obtained from deconvolution is 0.5 K. There is some potential for leakage by semidiurnal tides when difference fields are not separated by exactly 12 h. However, their effects on the difference-squared profiles (T_m^2) that form the basis for the deconvolution of the nonmigrating diurnal tides are generally less than 5% at the equator, where the temporal separation for SABER is roughly 9 h. This is due to the relatively weak amplitudes of nonmigrating semidiurnal tides below 90 km [Forbes *et al.*, 2008].

Figure 1 shows an example of DW2 determined via deconvolution for January–February 2005. The vertical coordinate is scaled height, or z/H , which is equivalent to $-\log(P/P_0)$ with a value of 1000 hPa used for P_0 . (In the upper stratosphere and mesosphere, a geometric height z can be estimated from scaled height using a value of 6.5 km for H .) We immediately note in Figure 1 the high degree of variability within the 2 month

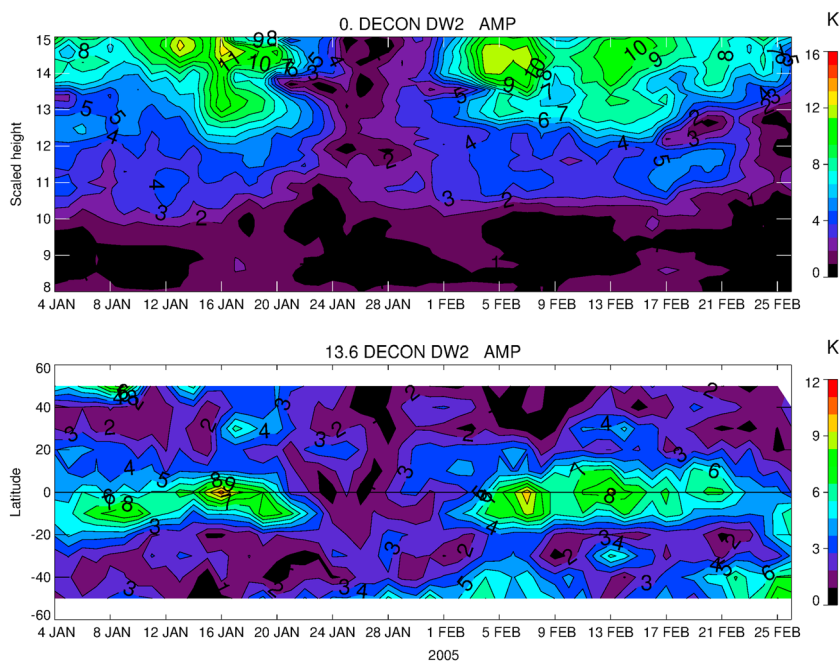


Figure 1. (top) Time versus scaled height of SABER DW2 temperature amplitude at the equator during January–February 2005. (Multiply z axis values by 6.5 to obtain approximate geometric height.) (bottom) Time versus latitude of SABER DW2 temperature amplitude at 13.6 scaled heights (90 km) during January–February 2005.

span that would be averaged out of a 60 day, 24 h-based tidal determination. Strong-amplitude periods during mid-January and in February are separated by a near absence of DW2 between 20 January and 1 February. Amplitudes at the equator grow rapidly above 11 scaled heights, exceeding 10 K by 14 scaled heights. Figure 1 (bottom) indicates that DW2 temperatures generally maximize at tropical latitudes, although an extratropical presence is suggested in early January and in the month of February. DS0, another DW1-PW1 interaction product, is shown for the same time period in Figure 2. Relative to DW2, DS0 amplitude is weaker at the equator and stronger (~9 K) in the Southern Hemisphere subtropics. Like DW2, this wave is also highly variable in time during January–February.

2.2. MLS

MLS was launched in July 2004 on the NASA Aura satellite and started full-up science operations on 13 August. The instrument measures temperature and geopotential height as well as various chemical constituents during day and night [Waters *et al.*, 2006]. The Aura orbit is Sun-synchronous with an ascending (north going) equator-crossing time near 1:30 P.M., a 98.8 min period, and a descending node crossing time near 1:30 A.M. The data coverage spans 82°S to 82°N on every orbit. The EOS MLS instrument retrieves useful temperatures from the troposphere up to about 0.001 hPa (about 94 km) [Schwartz *et al.*, 2008; Livesey *et al.*, 2013]. The precision of an individual profile is about 0.6 K at 10 hPa, increasing to 2.5 K at 0.001 hPa. The EOS MLS geophysical parameter data products are available at the NASA Goddard Earth Sciences Distributed Active Archive Center. This study used version 3.3.

MLS data are valuable to this study because of their temporal continuity, concurrence with SABER data and the zonal wave number decomposition enabled by their global extent. A novel aspect of the present study is the isolation of the spectral products of DW1-PW1 interaction (DW2 and DS0) in the MLT. The absence of local time precession in the Aura orbit precludes the determination of tides in MLS data. However, a proxy for the diurnal tide can be inferred from ascending-descending node (nearly 12 h) MLS temperature differences [Meek and Manson, 2009] that provide independent corroboration of the day-to-day variations in DW2 and DS0 reported here in SABER for the very first time.

Analysis of MLS temperature begins with the formation of global ascending-descending node differences. Both DS0 and DW2 are aliased to the zonal wave number 1 component of the ascending-descending node

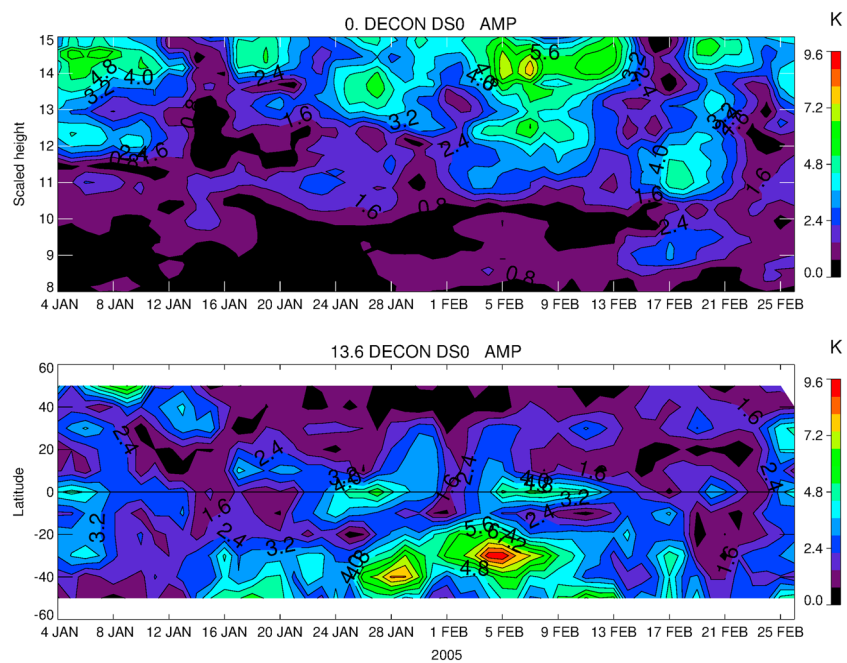


Figure 2. (top) Time versus scaled height of SABER DS0 temperature amplitude at the equator during January–February 2005. (Multiply z axis values by 6.5 to obtain approximate geometric height.) (bottom) Time versus latitude of SABER DS0 temperature amplitude at 13.6 scaled heights (90 km) during January–February 2005.

satellite temperature difference [Lieberman, 1991; Oberheide et al., 2002]. Consequently, we extract the zonal $m = 1$ component; this result is hereafter called the “MLS tidal proxy.” Next, the SABER retrievals of DW2 and DS0 are mapped to the local times and longitudes reported in MLS Level 2 files. We then form the difference of the ascending and the descending node mappings that can be directly compared with the MLS tidal proxy.

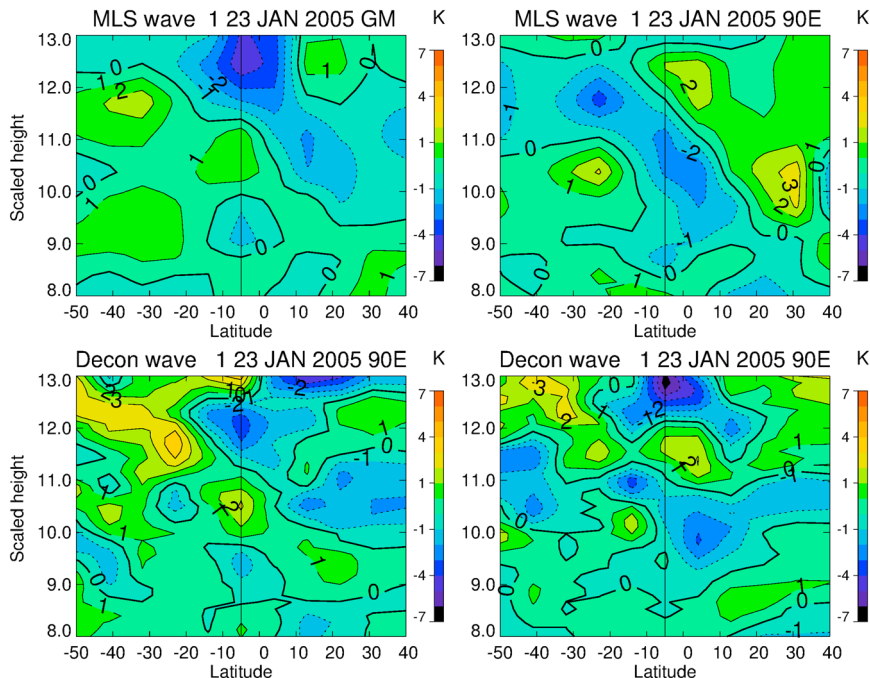


Figure 3. (top row) Latitude versus scaled height of the zonal wave number one component of the MLS ascending-descending node temperature difference computed from 5 days centered about 23 January 2005. (Multiply z axis values by 6.5 to obtain approximate geometric height.) (bottom row) SABER DW2 and DS0 mapped to MLS coordinates. (left column) Mapped at GM. (right column) Mapped at 90°E.

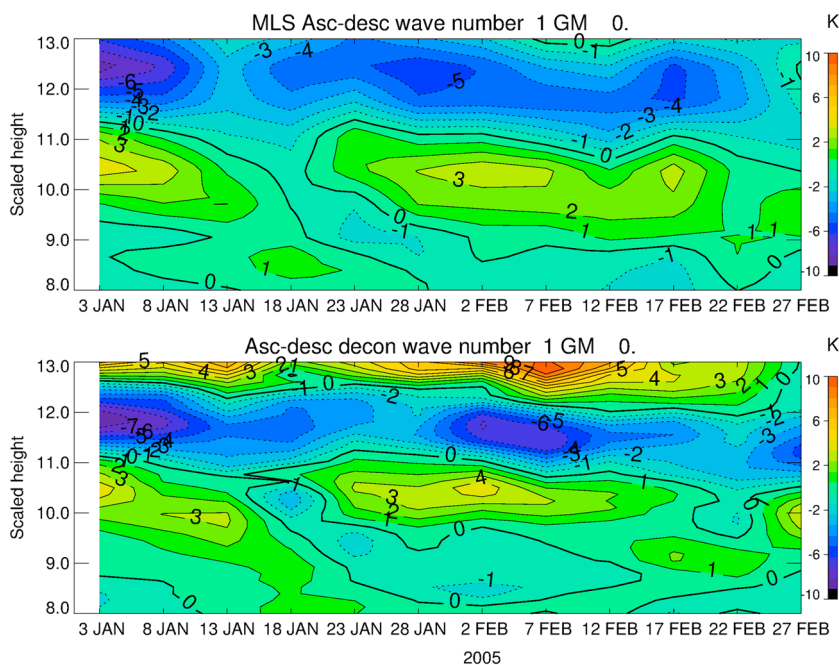


Figure 4. (top) Time versus scaled height of zonal wave number 1 component of the MLS ascending-descending node temperature at GM at the equator during January–February 2005. (Multiply z axis values by 6.5 to obtain approximate geometric height.) (bottom) SABER DW2 and DS0 mapped to MLS coordinates at GM at the equator.

Figure 3 compares typical latitude-altitude structures of $m = 1$ ascending-descending node difference in MLS and in SABER computed from daily DS0 and DW2 recoveries averaged over a 5 day interval centered on 23 January 2005. Overall, the two fields are in very good agreement. The mapping reconstructed from SABER DW2 and DS0 (Figure 3, bottom row) exhibits stronger amplitudes and more detailed structure. The vertical wavelength of the MLS diurnal proxy lengthens with height above 11 scaled heights, as observed at Greenwich meridian (GM) (Figure 3, top left). This behavior likely reflects the loss of MLS signal at the highest altitudes (~ 14 scaled heights) due to the increase with height of MLS's vertical averaging kernels [Schwartz *et al.*, 2008].

Figure 4 compares the temporal evolution of the MLS tidal proxy ($m = 1$ component of the ascending-descending node temperature difference) with that evaluated from the SABER DW2 and DS0 combination. Both data sets show nearly identical week-to-week variations below 12 scaled heights. Above this level, some differences are observed. For example, MLS shows peak minimum values of -5 K centered on 28 January and 17 February, while SABER's values are closer to -3 K and lie between peak minimum values. The reasons for these differences cannot be definitely established. However, it should be borne in mind that unlike the MLS difference pattern, the SABER differences have been constructed from DW2 and DS0 values obtained via deconvolution and mapped to MLS longitudes and local times. The deconvolution method is based upon interpolation between maxima and minima of the SABER ascending-descending node difference pattern, squared [Oberheide *et al.*, 2002]. As such, SABER DW2 and DS0 values include information from higher altitudes that is not reflected in the MLS difference pattern, which may account for some of the discrepancies above 12 scaled heights.

2.3. NOGAPS ALPHA

In order to explore quantitatively the relationships between DW1, PW1, DW2, and DS0, we require tidal horizontal winds. Winds are not observed by SABER or MLS. To obtain them, we turn to the Navy Operational Global Atmospheric Prediction System (NOGAPS) that has been extended up to 95 km (ALPHA: Advanced Level Physics High Altitude). NOGAPS ALPHA was developed as a prototype vertical extension of the Navy's operational-forecast model. This vertical extension required inclusion of additional stratospheric and mesospheric physical parameterizations, including radiative heating and cooling rates that account for nonlocal

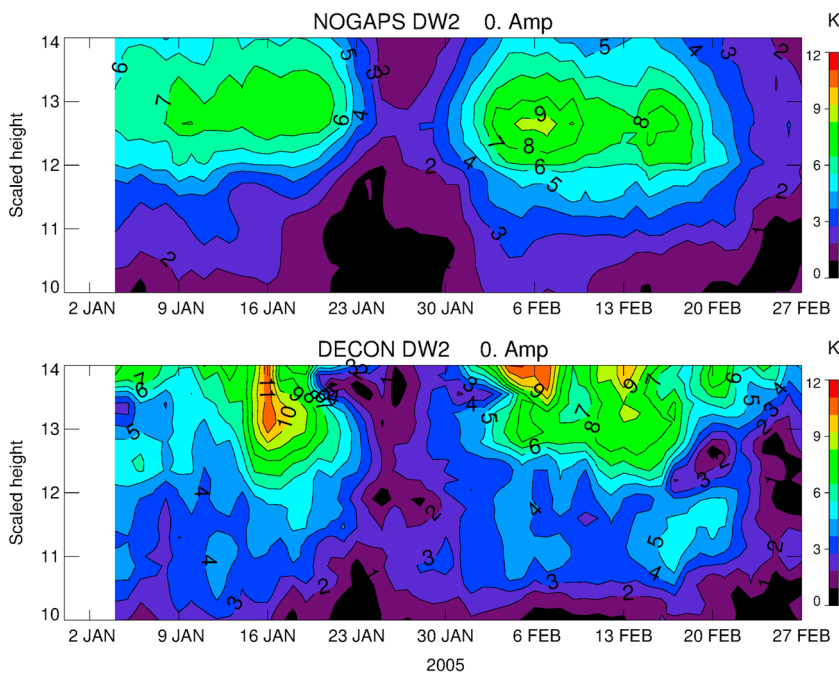


Figure 5. (top) Time versus scaled height of NOGAPS ALPHA DW2 temperature amplitude at the equator during January–February 2005. (Multiply z axis values by 6.5 to obtain approximate geometric height.) (bottom) Same as Figure 5 (top), showing SABER DW2 obtained via deconvolution. Tidal values are computed from sliding 4 day samples.

thermodynamic equilibrium, ozone and water vapor transport and photochemistry, and nonorographic gravity wave drag [Garcia *et al.*, 2007; Eckermann *et al.*, 2009].

The data assimilation component of NOGAPS ALPHA is the Naval Research Laboratory Atmospheric Variational Data Assimilation System (NAVDAS). NAVDAS is a 3D-variational system with a 6-hourly update cycle that assimilates both conventional meteorological data as well as data from MLS (temperature, ozone, and H₂O) and SABER temperatures. These analyses realistically describe the large-scale circulation below 100 km down to periods near 12 h [Eckermann *et al.*, 2009; Coy *et al.*, 2009; Siskind *et al.*, 2011; McCormack *et al.*, 2009, 2010; Nielsen *et al.*, 2010; Stevens *et al.*, 2010]. One limitation of NAVDAS is that the 6-hourly update cycle may alias semidiurnal and higher-order tidal modes. To circumvent this, a version of the NOGAPS ALPHA forecast model was configured to be initialized by the assimilation every 6 h [Siskind *et al.*, 2012] and provide output on an hourly cadence. This product allows global definitions of diurnal, semidiurnal, and higher-order tidal harmonics on a day-to-day or at least week-to-week basis. Hourly NOGAPS ALPHA output is available in January–February 2005, 2006, 2008, 2010, and for all months in 2009.

Diurnal tides are computed from NOGAPS ALPHA data as the space-time Fourier harmonics of 24 h composite time series constructed from sliding 4 day sequences. PWs are determined as the stationary (time mean) component of the Fourier harmonics of 4 day sequences computed from the NAVDAS 6-hourly analyses. Of the nonmigrating tides we are interested in, the DW2 response in NOGAPS ALPHA is overwhelmingly the strongest and most coherent in the mesosphere. We therefore confine our subsequent discussions of tide-PW interaction products to DW2.

Figure 5 shows a typical comparison of the altitude-time structure of DW2 derived from NOGAPS ALPHA hourly forecasts (top) and sliding 4 day averages of SABER values obtained via deconvolution. The weekly evolution of DW2 during January–February is similar in both data sets, but the SABER retrievals generally show more structure and higher-amplitude maxima (for example, on 16 January and 6 February). In addition to a “smearing” of resolved waves in time and space, another feature of the NOGAPS ALPHA wave definitions is the attenuation of amplitudes above 13 scaled heights (~87 km). Accompanying this amplitude reduction is a lengthening of vertical wavelength, illustrated in Figure 6. These behaviors are likely due to the inclusion

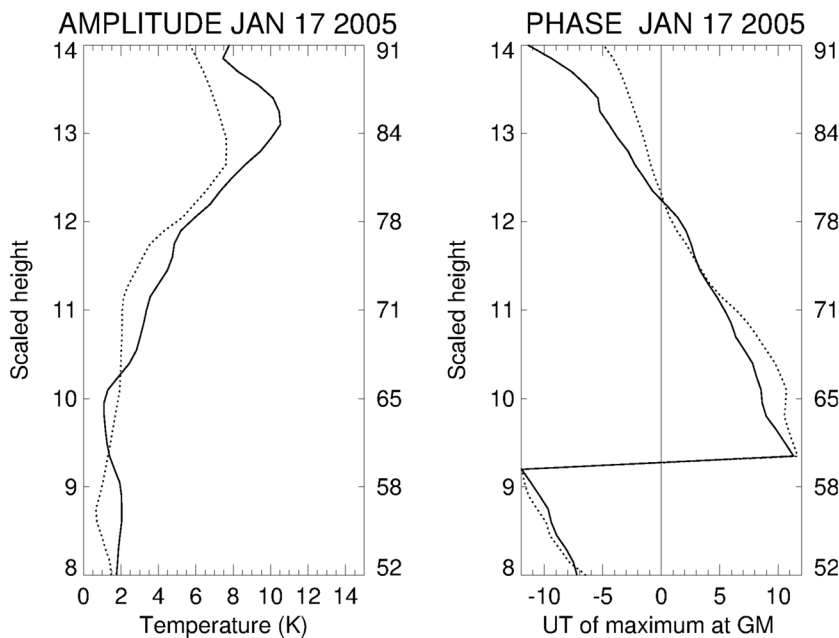


Figure 6. (left) Amplitude and (right) phase of DW2 at the equator over a 4 day interval centered on 17 January 2005. Dotted curves, NOGAPS ALPHA; Solid curves, SABER. Right axis labels are approximate geometric altitudes.

of MLS temperature in the data sources assimilated by NOGAPS ALPHA. There is also additional damping imposed near the top boundary of the model (~ 100 km).

Below 13.5 scaled heights, NOGAPS ALPHA generally tracks the week-to-week amplitude evolution seen in SABER, albeit more smoothed. This property is illustrated in a typical example shown in Figure 7. NOGAPS ALPHA identifies sustained DW2 episodes at 13.4 scaled heights centered on the equator during most of

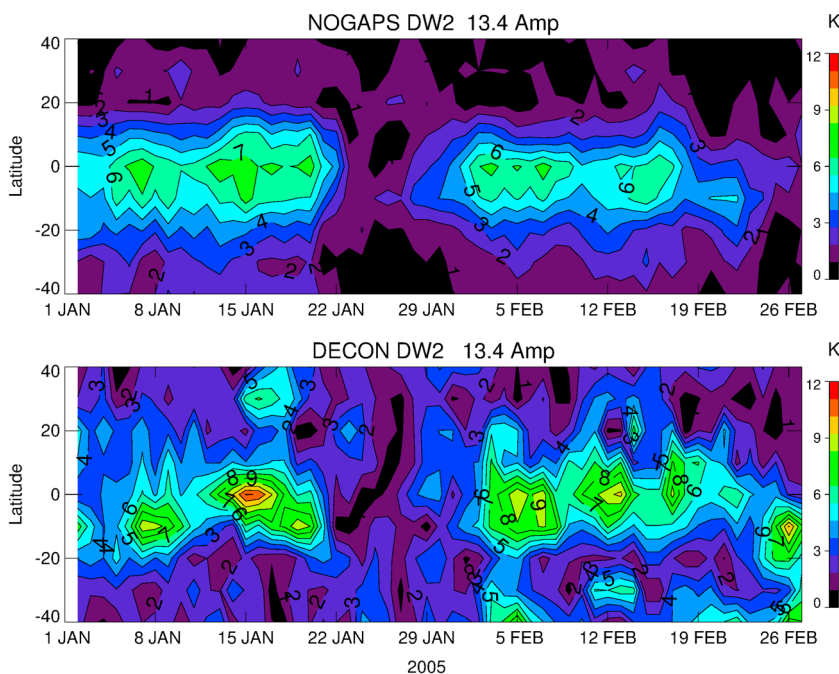


Figure 7. (top) Time versus latitude of NOGAPS ALPHA DW2 temperature amplitude at 13.4 scaled heights (~88 km) during January–February 2009. (bottom) The same as Figure 7 (top), showing SABER amplitudes obtained via deconvolution. Tidal values are computed from sliding 4 day samples.

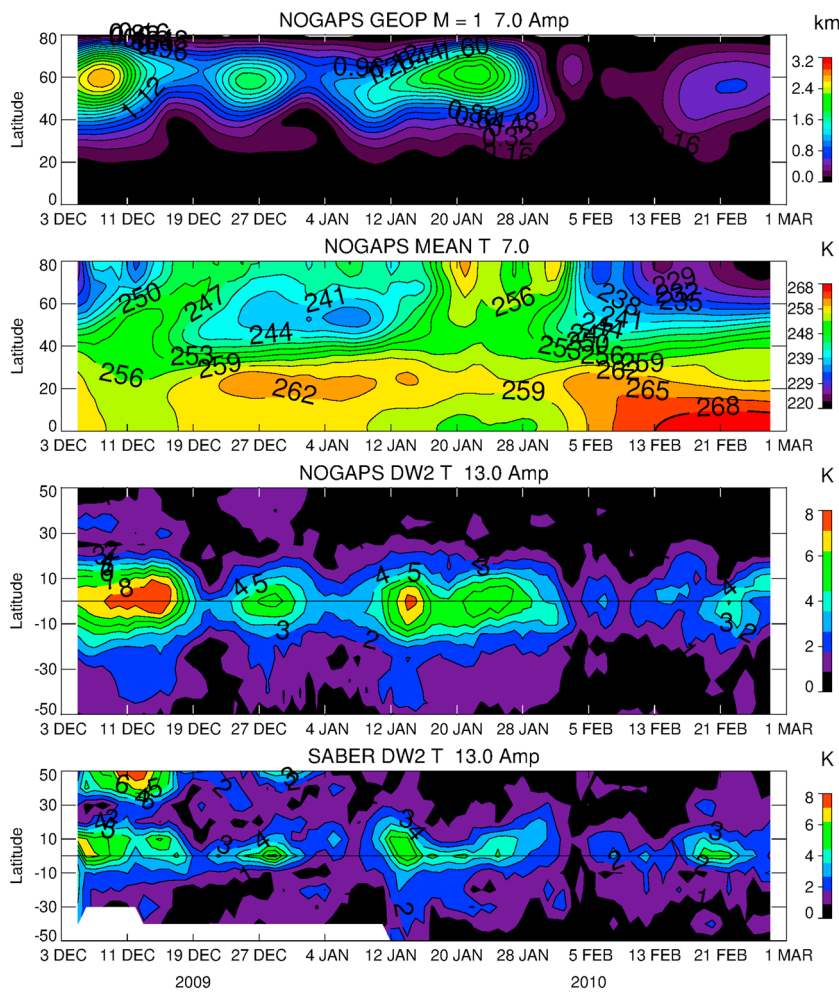


Figure 8. Latitude versus time variations in NOGAPS ALPHA parameters during December 2009–February 2010. (first panel) PW1 geopotential height amplitude at seven scaled heights (~ 48 km), in kilometer. (second panel) \bar{T} . (third panel) NOGAPS ALPHA DW2 T amplitude at 13 scaled heights (~ 87 km). (fourth panel) SABER DW2 T amplitude at 13 scaled heights.

January and February 2005, with a relative absence between 22 and 29 January. DW2 amplitudes obtained via deconvolution show similar low-latitude structure in January but with stronger maxima and also exhibit an amplitude maximum at 30°N that does not appear in NOGAPS ALPHA. In February, four separate low-latitude maxima are identified in SABER DW2, which are coalesced into two maxima in NOGAPS ALPHA. High-latitude extensions of SABER DW2 to 40°S on 5 February and 26 February are not captured in NOGAPS ALPHA.

A possible source of some of the discrepancies between NOGAPS ALPHA and SABER DW2 lies in the differences in the vertical structure and extent of NOGAPS ALPHA relative to the SABER data set. As previously noted, the weaker DW2 amplitudes in NOGAPS ALPHA likely occur in part due to damping near the model upper boundary. The deconvolution method by design results in SABER DW2 values that are influenced by the structure above (and below) the levels of the DW2 retrievals themselves. Thermospheric wind analyses by Lieberman *et al.* [2013] indicate that DW2 maintains significant amplitude to at least 110 km. Thus, it might be expected that amplitudes of DW2 recovered from SABER via deconvolution will exceed those recovered from assimilated data approaching the “sponge” (damping) layers.

We conclude that DW2 derived from NOGAPS ALPHA hourly analyses at low latitudes up to 13.5 scaled heights captures the essential structural and temporal features observed in SABER during the periods of interest for this study. Therefore, we shall use NOGAPS ALPHA diurnal horizontal winds and temperature for investigating DW2-PW interaction.

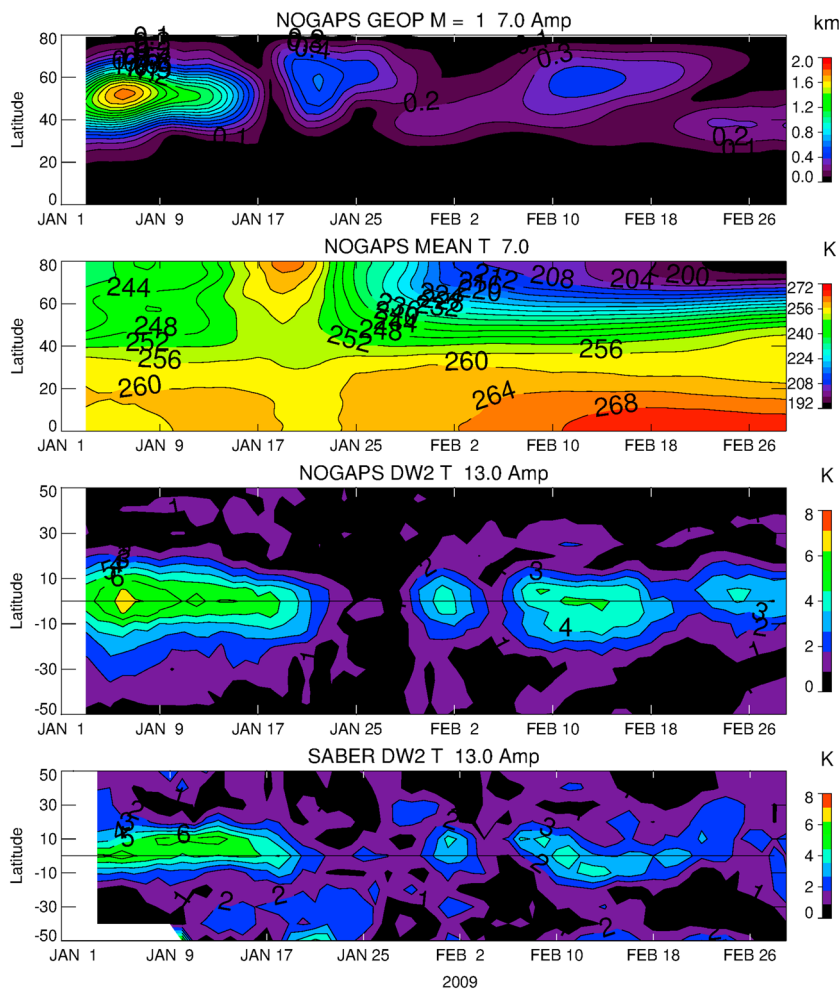


Figure 9. As in Figure 8 but for January–February 2009.

3. Evolution of PW1 and DW2 During Winter Months

The previous sections established reasonable similarity between DW2 derived from SABER and from NOGAPS ALPHA hourly forecasts up to about 90 km. In this section we examine the short-term variability of NOGAPS ALPHA DW2 in relation to PW1 activity during several winter seasons.

Figure 8 shows the evolution of stratospheric PW1 geopotential height amplitude, zonal mean temperature (\bar{T}), and mesospheric DW2 T amplitude during December 2009 to February 2010. PW1 amplitudes are very strong at high northern latitudes in early December and late January, with a weaker secondary maximum in late December. (PW1 geopotential height in the summer hemisphere is nonexistent and is not shown.) Following the strong PW1 event in early December, a weak stratospheric warming is observed poleward of 60°N. A much stronger warming follows the PW1 maximum in late January. Mesospheric NOGAPS ALPHA DW2 temperature (Figure 8, third panel) maximizes near the equator, and its evolution often appears to track the PW1 amplitudes. For example, a strong-amplitude DW2 episode with an 8 K maximum lasts from 6 December to 18 December. A secondary maximum of about 6 K appears in the final week of December. DW2 amplitudes increase again (> 6 K) between the middle and the end of January. A final maximum of 5 K is observed between 24 and 28 February, although the PW1 amplitude is very weak. SABER DW2 amplitudes are shown in Figure 8 (fourth panel) for comparison with NOGAPS ALPHA. Agreement at low latitudes is generally quite good, with slightly higher maxima in SABER. A secondary high-altitude maximum in early December is significantly stronger in SABER than in NOGAPS ALPHA.

PW1 geopotential height and DW2 T amplitudes also appear to be highly correlated during January–February 2009, as illustrated in Figure 9. The primary PW1 amplitude maximum occurred in the midlatitude stratosphere

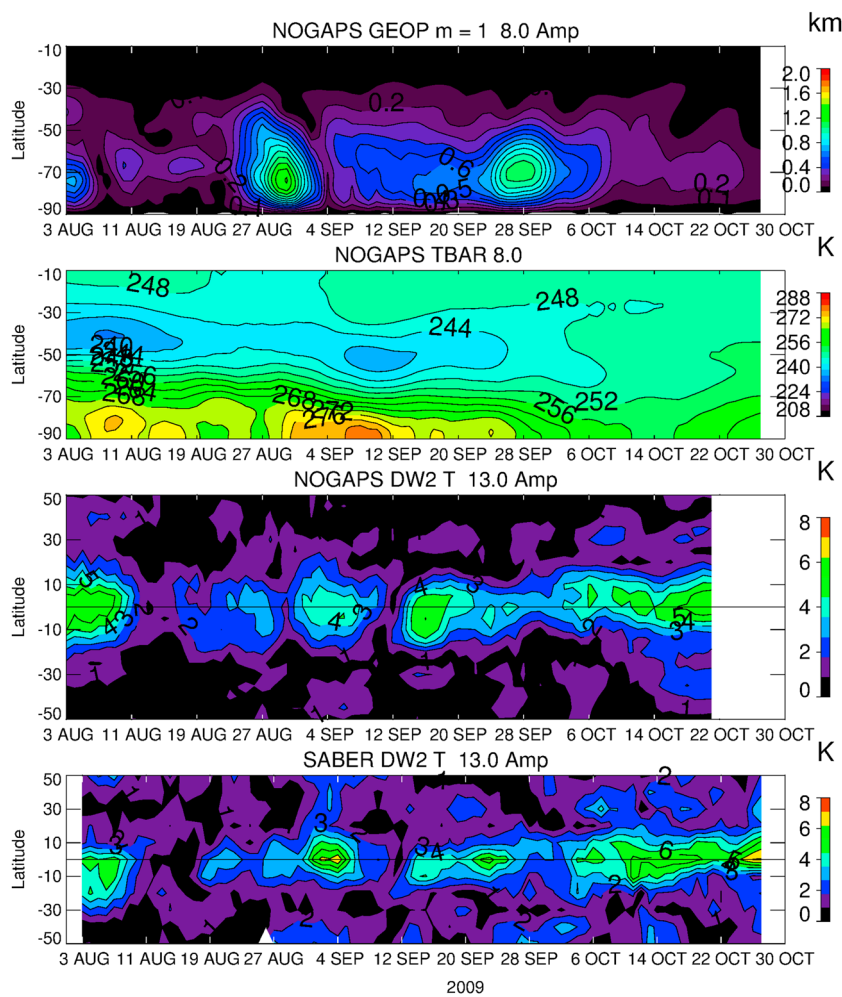


Figure 10. As in Figure 8 but for August–October 2009 in the Southern Hemisphere.

in early January. \bar{T} warming maximizes on 17 January, possibly in response to amplification and breakdown of PW2 (not shown). NOGAPS and SABER DW2 T amplitudes are very similar and highest (6 K) during the first week in January when PW1 was also strong. However, significant DW2 amplitudes persist until 17 January and also appear in February (5 K) when PW1 was quite weak in the stratosphere. Qualitatively similar relationships between DW2 and PW1 are also observed in the months of January and February for the years of 2005, 2006, and 2008 (not shown). Thus, the DW2 evolution in the mesosphere is generally associated most clearly with the stratospheric and mesospheric PW1 amplitudes, as opposed to \bar{T} . The relationship is not a linear one; similar DW2 amplitudes are often observed in the presence of strong and weak PW1.

During 2009, NOGAPS ALPHA hourly forecasts are available during the Southern as well as the Northern Hemisphere winter. Figure 10 shows the evolution of PW1, \bar{T} , and NOGAPS and SABER DW2 T amplitude during August–October 2009, the only months when significant Southern Hemisphere PW1 amplitudes were observed. Strong-amplitude PW1 events occur in late August–early September and in early October. High-latitude warming is observed during roughly 12 September–14 October. However, the associations between PW1 and DW2 are not as clear as we have seen in the Northern Hemisphere. The strongest DW2 amplitudes are observed in early August, 20 September, and 25 October, which are days when PW1 amplitudes were quite weak. A secondary DW2 response does occur after 4 September, which may be associated with the strong PW1 at the end of August.

The Eliassen-Palm (EP) flux vector (F^ϕ, F^z) is a wave diagnostic whose orientation is parallel to the group velocity and whose divergence (convergence) per unit mass—a measure of wave stress—indicates a source

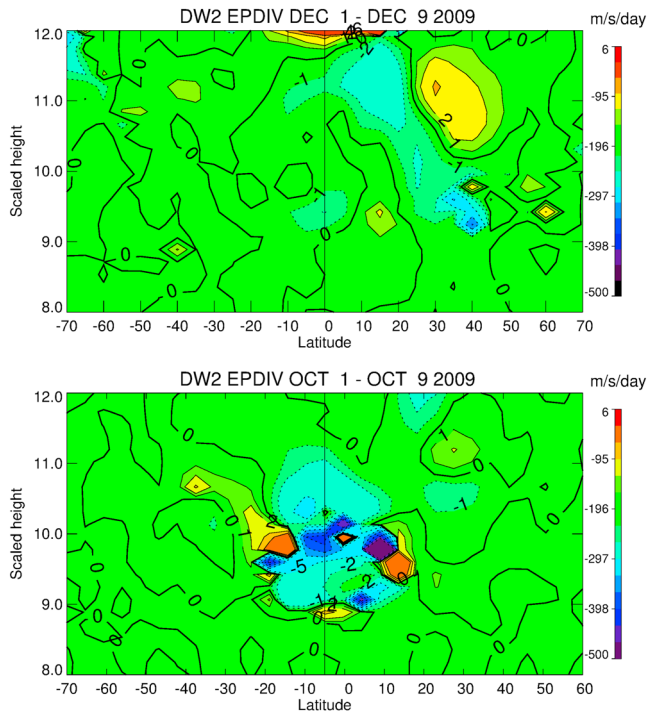


Figure 11. Eliassen-Palm flux divergence per unit mass (in $\text{m s}^{-1} \text{ d}^{-1}$) averaged between (top) 1–9 December and (bottom) 1–9 October 2009.

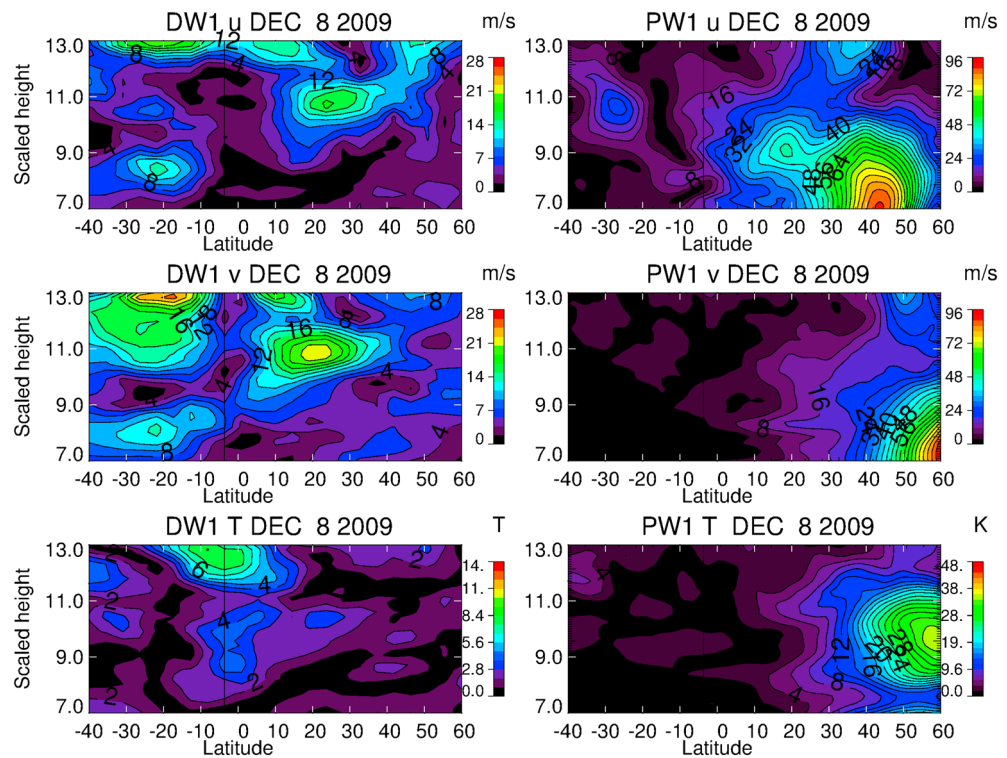


Figure 12. (left column) Latitude versus scaled height of (top) DW1 u' in m s^{-1} , (middle) v' (in m s^{-1}), and (bottom) T' on 8 December 2009. (right column, top) PW1 u' (in m s^{-1}), (middle) v' (in m s^{-1}), and (bottom) T' on 8 December 2009.

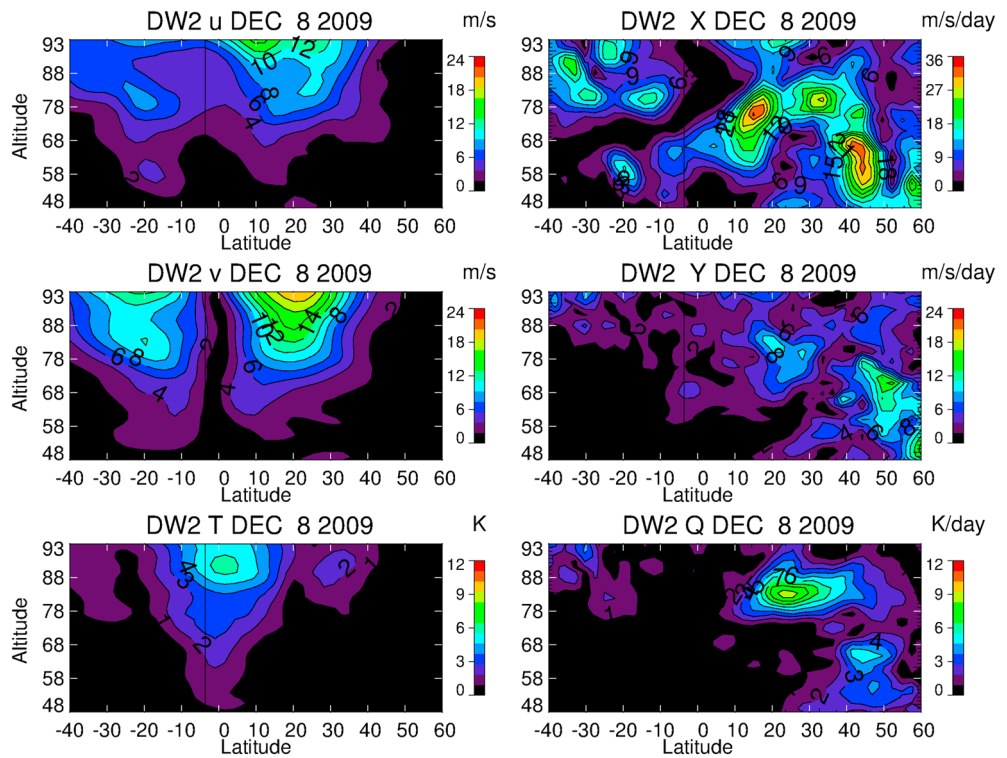


Figure 13. (left column) Latitude versus scaled height of DW2 (top) u' , (middle) v' , and (bottom) T' on 8 December 2009. (right column, top) DW2 X , (middle) Y , and (bottom) Q on 8 December 2009. Units of X and Y are $\text{m s}^{-1} \text{d}^{-1}$. Units of Q are K d^{-1} .

(sink) region [Andrews et al., 1987]. EP flux vector components were calculated using DW2 temperatures and winds computed from NOGAPS hourly forecasts, according to

$$F^\phi = \rho_0 a \cos \phi (\bar{U}_z v' \theta' / \bar{\theta}_z - \bar{v}' u') \quad (1)$$

$$F^z = \rho_0 a \cos \phi \left\{ \left[f - (a \cos \phi)^{-1} (\bar{U} \cos \phi)_\phi \right] \bar{v}' \theta' / \bar{\theta}_z - \bar{w}' u' \right\} \quad (2)$$

$$\nabla \cdot F = (a \cos \phi)^{-1} \frac{\partial}{\partial \phi} (F^\phi \cos \phi) + \frac{\partial F^z}{\partial z} \quad (3)$$

[Andrews et al., 1987]. ρ_0 is the basic state density; θ is potential temperature; u' , v' , and w' are perturbation zonal, meridional, and vertical winds; ϕ is latitude; f is the Coriolis parameter; and a is Earth radius. The z and ϕ subscripts denote the vertical and meridional gradients, respectively.

Figure 11 compares DW2 EP flux divergence per unit mass for two periods of contrasting PW1 activity. The top panel shows the divergence per unit mass averaged over 1–9 December 2009, when both strong DW2 and middle-high latitude PW1 were observed (see Figure 8). Figure 11 (bottom) shows the same quantities averaged between 1 and 9 October 2009, when DW2 is strong and a PW1 at high southern latitudes is waning. DW2 EP flux is convergent in the upper stratosphere-lower mesosphere and concentrated at low latitudes. This behavior is consistent with DW2 being predominantly forced by tropospheric sources [Hagan and Forbes, 2002] and subject to damping above the stratosphere. When PW1 is strong at middle and high latitudes (December), the EP flux divergence pattern forms a dipole tilting equatorward and upward, with the divergence (convergence) on the poleward (equatorward) flank. The orientation of the dipole is similar to the EP flux vector of a vertically propagating quasi-stationary PW [Hamilton, 1982]. The parallels between PW and DW2 EP flux divergence patterns in December and the contrast with the October pattern suggest a midlatitude, PW1-related source of DW2.

A leading challenge in interpreting the evolution of DW2 in the presence of PW1 lies in the fact that DW2 has perpetual tropospheric sources in addition to tide-PW interaction. Thus, the specific contributions of tide-PW forcing to DW2 can only be isolated through numerical modeling. We explore this forcing in the following section.

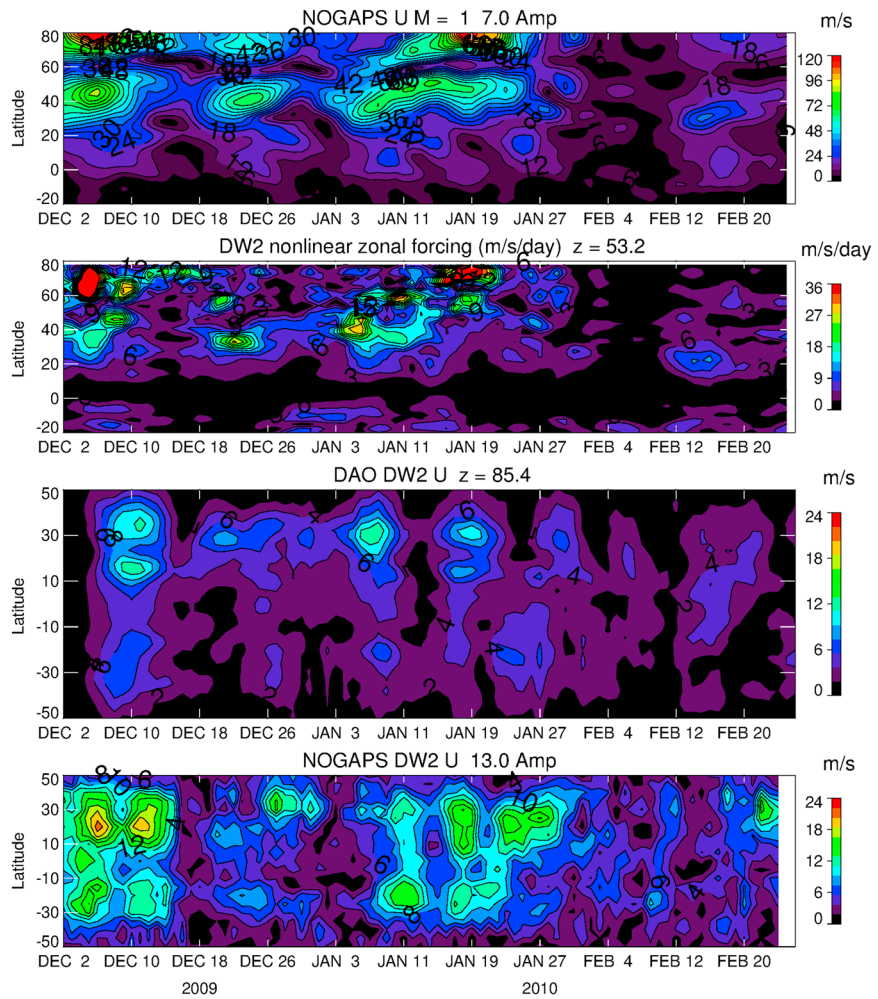


Figure 14. Latitude versus time variations during December 2009–February 2010. (first panel) PW1 u' amplitude between 20°S and 70°N at seven scaled heights (~48 km). (second panel) DW2 X amplitude between 50°S and 70°N at 53 km. (third panel) DW2 u' modeled amplitude between 50°S and 50°N at 13 scaled heights (~85 km), forced only by DW1-PW1 interaction. (fourth panel) NOGAPS DW2 u_t amplitude between 50°S and 50°N at 13 scaled heights.

4. Nonlinear Forcing

We employ a primitive equation (PE) model described in *Ortland and Alexander [2006]* to quantify the contribution to DW2 from nonlinear forcing. Longitude structure is represented by Fourier coefficients from zonal wave number $s = 0 – 4$, and 40 Legendre polynomial coefficients represent the latitude structure. A vertical grid extending from the surface to 130 km is used with a spacing of 1 km. Zonal mean winds and temperatures are initialized to those in NOGAPS ALPHA. Temperatures are relaxed back to the initial zonal mean state with Newtonian cooling at a rate of $.05 \text{ day}^{-1}$. Rayleigh friction above 110 km is used as a crude representation of ion drag and also prevents wave reflection from the model top.

Waves are produced by specified forcing terms in the zonal, meridional, and potential temperature tendency equations. Nonlinear tidal forces arise from centripetal acceleration, horizontal advection of tidal momentum and potential temperature by PW winds (u_p, v_p), and horizontal advection of (u_p, v_p) and Θ_p by tidal winds (u_t, v_t). These forces are represented by the following equations for nonlinear zonal (X_t) and meridional (Y_t) tidal forcing, and tidal adiabatic heating (Q_t):

$$X_t = -\frac{u_p}{a \cos \phi} \frac{\partial u_t}{\partial \lambda} - \frac{u_t}{a \cos \phi} \frac{\partial u_p}{\partial \lambda} - \frac{v_p}{a} \frac{\partial u_t}{\partial \phi} - \frac{v_t}{a} \frac{\partial u_p}{\partial \phi} - \frac{u_t \tan \phi}{a} v_p - \frac{u_p \tan \phi}{a} v_t \quad (4)$$

$$Y_t = -\frac{u_p}{a \cos \phi} \frac{\partial v_t}{\partial \lambda} - \frac{u_t}{a \cos \phi} \frac{\partial v_p}{\partial \lambda} - \frac{v_p}{a} \frac{\partial v_t}{\partial \phi} - \frac{v_t}{a} \frac{\partial v_p}{\partial \phi} - 2 \frac{u_t \tan \phi}{a} u_p \quad (5)$$

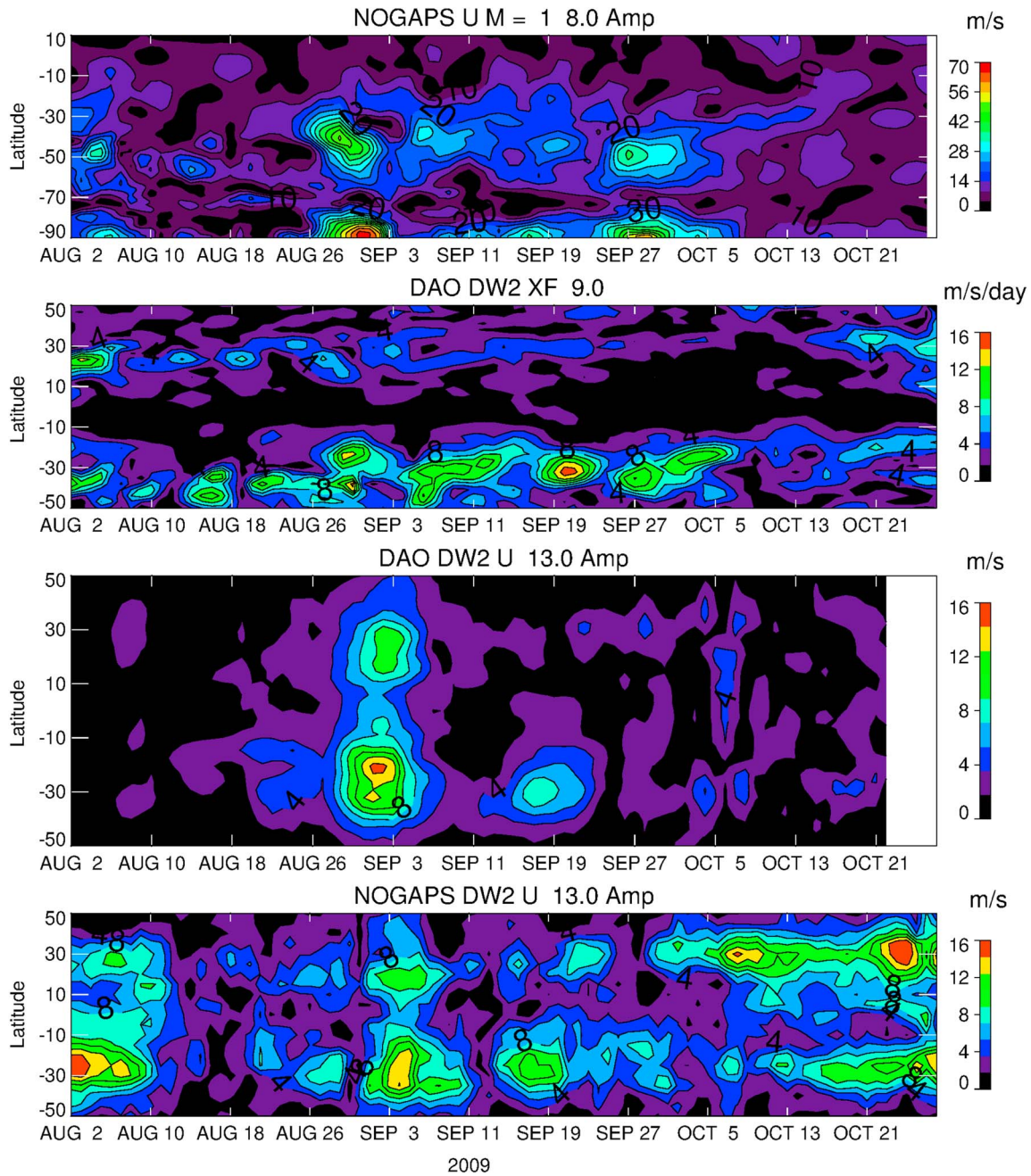


Figure 15. Latitude versus time variations during August-September-October 2009. (first panel) PW1 u' amplitude between 20°N and 90°S at eight scaled heights ($\sim 56\text{ km}$). (second panel) DW2 X amplitude between 50°S and 50°N at nine scaled heights ($\sim 62\text{ km}$). (third panel) Modeled DW2 u' amplitude between 50°S and 50°N at 13 scaled heights ($\sim 87\text{ km}$), forced only by DW1-PW1 interaction. (fourth panel) NOGAPS DW2 u' amplitude between 50°S and 50°N at 13 scaled heights.

$$Q_t = -\frac{u_p}{a \cos \phi} \frac{\partial \theta_t}{\partial \lambda} - \frac{u_t}{a \cos \phi} \frac{\partial \theta_p}{\partial \lambda} - \frac{v_p}{a} \frac{\partial \theta_t}{\partial \phi} - \frac{v_t}{a} \frac{\partial \theta_p}{\partial \phi} \quad (6)$$

NOGAPS ALPHA DW1 and PW1 temperatures and winds are used to compute the quantities in equations (4)–(6) that become sources of DW2 and DS0. Our focus is on the evolution of DW2.

Figure 12 shows DW1 and PW1 on 8 December 2009. This day represents a strong PW1 event at high northern latitudes. We first note that (right column) PW1 v' and T' are high-latitude winter features, while PW1 u' shows some penetration to the equator and even into the summer hemisphere. DW1 T' is confined to tropical

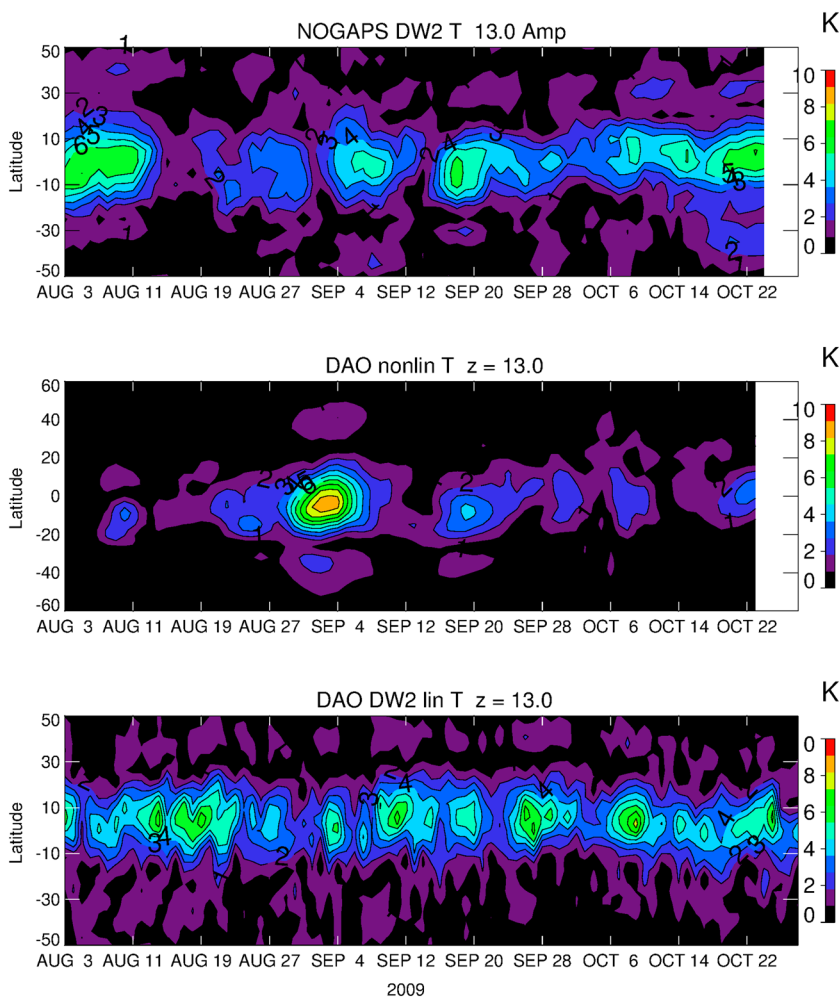


Figure 16. Latitude versus time variations during August–September–October 2009. (top) NOGAPS DW2 u' amplitude between 50°S and 50°N at 13 scaled heights (~87 km). (middle) Modeled DW2 u' amplitude between 50°S and 50°N at 13 scaled heights, forced only by DW1–PW1 interaction. (bottom) DW2 u' amplitude between 50°S and 50°N at 13 scaled heights, forced by solar and latent heating.

latitudes, while DW1 u' and v' extend to 40°N (left column). Thus, the most efficient nonlinear processes are expected to involve advection of PW1 u' by DW1 horizontal winds and advection of DW1 winds by PW1 u' .

This inference is borne out by Figure 13, showing DW2 on 8 December, and the corresponding X_t , Y_t , and Q_t . X_t dominates Y_t , due to the spatial overlap of PW1 u' and DW2 winds. Analysis of the individual terms in equation (4) (not shown) indicates that advection of PW1 u' by DW1 v' (the fourth term on the right-hand side) is the primary contributor to X_t equatorward of 40°N and in the Southern Hemisphere. While PW1 is largely a winter hemisphere feature, DW2—generated primarily through tidal advection of the low-latitude extension of PW1—is global, with a strong presence in the summer as well as in the winter hemisphere.

Figure 14 shows the evolution of nonlinearly generated DW2 (third panel) during December 2009–February 2010, together with PW1 u' at seven scaled heights (first panel), DW2 X at nine scaled heights, and NOGAPS ALPHA DW2 u' (fourth panel). We note that X , while generally stronger in the low-latitude winter hemisphere, is always present in the Southern Hemisphere low latitudes as well. Overall, nonlinearly forced DW2 tracks the observations in both hemispheres, albeit with weaker amplitudes. A close comparison of Figure 14 (first and third panels) shows that the nonlinearly generated DW2 peaks when the PW1 u' penetrates to the lowest latitudes. These events are centered on 5–12 December interval, 26 December, 7–11, 19, and 29 January, and 17 February. Nonlinearly generated DW2 maximizes between 10–14 December and on 8 and 19 January. The December events occur within the same time frame that DW2 maxima were observed in NOGAPS ALPHA (Figure 14, fourth panel) during the first half of December, although the modeled 8 and 19 January maxima

precede the NOGAPS ALPHA DW2 by 1–2 days. Thus, DW2 can be considered a marker of the extension of wintertime PW1 activity to low latitudes.

Figure 15 illustrates that the PW1-DW1 coupling mechanism also operates during the Southern Hemisphere winter. Three PW1 events occurred in the austral winter of 2009: Late August–early September, 17 September, and late September–early October. The most significant nonlinear response to PW1-DW1 forcing occurs in response to the early September event, facilitated by X between 20 and 40°S. A secondary nonlinear DW2 maximum is centered on 19 September. However, despite the strong PW1 event centered on 27 September, mesospheric DW2 in NOGAPS ALPHA is very weak between 22 September and 5 October, and no DW2 appears to be generated by DW1-PW1 interaction in the model during this interval. The reason for this absence can be traced to the confinement of PW1 u' to latitudes poleward of 20°S during the 27 September event. This results in virtually nonexistent meridional advection of PW1 u' by the DW1, which is the primary agent for nonlinear DW2 generation.

Strong DW2 amplitudes appear in NOGAPS in early August and during October, which do not arise from nonlinear forcing. Figure 16 compares NOGAPS ALPHA DW2 with the responses to nonlinear forcing and the combination of solar and latent heating. Heating accounts for a nearly continuous presence of DW2 in the Northern Hemisphere. However, the PE model response to heating is much weaker in the Southern Hemisphere and does not explain the high values of DW2 observed in the Southern Hemisphere between 3 and 10 August and the final week in October.

5. Summary and Conclusions

We have examined short-term variability in DW2 and DS0, key nonmigrating diurnal tides predicted from interactions between DW1 and PW1. Our first step was to isolate significant day-to-day variability of these components during winter months in SABER temperatures using a deconvolution method. Validation was carried out by mapping the SABER retrievals of DW2 and DS0 to the coordinates of concurrent EOS MLS sampling. Ascending-descending node temperature differences (a tidal proxy) were then formed from the MLS data and the mappings of SABER DW2 and DS0. We determined that the behavior of the convolved DW2 and DS0 waves in SABER was very similar to the characteristics of an MLS tidal proxy below 85 km. Above this level, MLS retrievals attenuate, resulting in lower tidal amplitudes and somewhat longer vertical wavelengths compared to SABER. Finally, we also validated the SABER retrievals of DW2 with those recovered from hourly forecasts of NOGAPS ALPHA.

DW2 amplitudes near 90 km are observed concurrently with strong stratospheric PW1. Patterns of DW2 EP flux divergence per unit mass (indicative of a wave source) at middle and high winter latitudes in the upper stratosphere further point to PWs as a tidal source. NOGAPS ALPHA winds and temperatures enabled computation of advection among tidal and PW1 winds and temperatures. These terms were input as forcing to a PE model, in order to quantify the DW2 resulting from DW1-PW1 interaction. The model results provide convincing support for DW1 advection of PW1 momentum as a source of DW2 during winter months.

Our modeling experiments also highlight mechanisms for vertical and interhemispheric coupling via tide-PW interaction. While stationary PWs are primarily a midlatitude wintertime phenomenon in the stratosphere, they are ducted upward and equatorward, facilitating their interaction with low-latitude DW1 winds. The tidal products of the interaction are vertically propagating waves with a global extent. Our modeling experiments explicitly demonstrate that DW2 variability observed at a single point in the high-altitude summer hemisphere may originate in PW1 sources in the winter hemisphere.

References

- Andrews, D. G., J. R. Holton, and C. B. Leovy (1987), *Middle Atmosphere Dynamics*, Academic Press, Orlando, Fla.
- Angelat i Coll, M., and J. M. Forbes (2002), Nonlinear interactions in the upper atmosphere: The $s = 1$ and $s = 3$ nonmigrating semidiurnal tides, *J. Geophys. Res.*, 107(A8), 1157, doi:10.1029/2001JA900179.
- Canziani, P. O. (1994a), On tidal variability and the existence of planetary-scale wave-like oscillations in the upper thermosphere. 1. Observations of tidal variability, *J. Atmos. Terr. Phys.*, 56, 901–912.
- Canziani, P. O. (1994b), On tidal variability and the existence of planetary-scale wave-like oscillations in the upper thermosphere. 2. Nonlinear-interactions and global-scale oscillations, *J. Atmos. Terr. Phys.*, 56, 913–930.
- Chapman, S., and R. S. Lindzen (1970), *Atmospheric Tides*, Gordon and Breach, New York.
- Chau, J. L., B. G. Fejer, and L. P. Goncharenko (2009), Quiet variability of equatorial E × B drifts during a sudden stratospheric warming event, *Geophys. Res. Lett.*, 36, L05101, doi:10.1029/2008GL036785.

Acknowledgments

The authors wish to thank the TIMED SABER and EOS MLS science and data processing teams for their careful study, validation, and processing of the SABER and MLS data sets. We thank our anonymous referees for their incisive reviews. SABER data can be accessed at http://saber.gats-inc.com/data_services.php. MLS data are distributed at <http://disc.sci.gsfc.nasa.gov/Aura/data holdings/MLS/index.shtml>. NOGAPS ALPHA data are archived at GATS Inc. and available upon request (ruth@gats-inc.com). This research was supported by NSF grant AGS-1243364, NASA contracts NNN12CF66C and NNX14AB15G to GATS, and interagency agreement NNN13AW41I to the Naval Research Laboratory.

- Chau, J. L., N. A. Aponte, E. Cabassa, M. P. Sulzer, L. P. Goncharenko, and S. A. Gonzalez (2010), Quiet time ionospheric variability over Arecibo during sudden stratospheric warming events, *J. Geophys. Res.*, 115, A00G06, doi:10.1029/2010JA015378.
- Coy, L., S. Eckermann, and K. Hoppel (2009), Planetary wave breaking and tropospheric forcing as seen in the stratospheric sudden warming of 2006, *J. Atmos. Sci.*, 66, 495–507.
- Eckermann, S. D., K. W. Hoppel, L. Coy, J. P. McCormack, D. E. Siskind, K. Nielsen, A. Kochenash, M. H. Stevens, C. R. Englert, and M. Hervig (2009), High-altitude data assimilation system experiments for the northern summer mesosphere season of 2007, *J. Atmos. Sol. Terr. Phys.*, 71, 531–551.
- Forbes, J. M., N. A. Makarov, and Y. I. Portnyagin (1995), First results from the meteor radar at South Pole: A Large 12-hour oscillation with zonal wavenumber one, *Geophys. Res. Lett.*, 22, 3247–3250.
- Forbes, J. M., M. Kilpatrick, D. Fritts, A. H. Manson, and R. A. Vincent (1997a), Zonal mean and tidal dynamics from space: An empirical examination of aliasing and sampling issues, *Ann. Geophys.*, 15, 1158–1164.
- Forbes, J. M., M. E. Hagan, X. Zhang, and K. Hamilton (1997b), Upper atmosphere tidal oscillations due to latent heat release in the tropical troposphere, *Ann. Geophys.*, 15, 1165–1175.
- Forbes, J. M., X. Zhang, S. Palo, J. Russell, C. J. Mertens, and M. Mlynczak (2008), Tidal variability in the ionospheric dynamo region, *J. Geophys. Res.*, 113, A02310, doi:10.1029/2007JA012737.
- Garcia, R. R., D. R. Marsh, D. E. Kinnison, B. A. Boville, and F. Sassi (2007), Simulation of secular trends in the middle atmosphere, 1950–2003, *J. Geophys. Res.*, 112, D09301, doi:10.1029/2006JD007485.
- Goncharenko, L., A. J. Coster, J. L. Chau, and C. E. Valladares (2010), Impact of sudden stratospheric warmings on equatorial ionization anomaly, *J. Geophys. Res.*, 115, A00G07, doi:10.1029/2010JA015400.
- Hagan, M. E., and J. M. Forbes (2002), Migrating and nonmigrating diurnal tides in the middle and upper atmosphere excited by tropospheric latent heat release, *J. Geophys. Res.*, 107(D24), 4754, doi:10.1029/2001JD001236.
- Hagan, M. E., and R. G. Roble (2001), Modeling diurnal tide variability with the National Center for Atmospheric Research thermosphere-ionosphere-mesosphere-electrodynamics general circulation model, *J. Geophys. Res.*, 106, 24,869–24,882.
- Hagan, M. E., J. L. Chang, and S. K. Avery (1997), Global-scale wave model estimates of nonmigrating tidal effects, *J. Geophys. Res.*, 102, 16,439–16,452.
- Hall, G. E., P. Namboothiri, A. H. Manson, and C. E. Meek (1995), Daily, tidal, planetary wave and gravity wave amplitudes over the Canadian prairies, *J. Atmos. Terr. Phys.*, 57, 1553–1567.
- Hamilton, K. (1981), Latent heat release as a possible forcing mechanism for atmospheric tides, *Mon. Weather Rev.*, 109, 3–17.
- Hamilton, K. (1982), Some features of the climatology of the Northern Hemisphere stratosphere revealed by NMC upper atmosphere analyses, *J. Atmos. Sci.*, 39, 2737–2749.
- Hernandez, G., G. J. Fraser, and R. W. Smith (1993), Mesospheric 12 hour oscillation near South Pole Antarctica, *Geophys. Res. Lett.*, 20, 1787–1790.
- Hitchman, M. H., and C. B. Leovy (1985), Diurnal tide in the equatorial middle atmosphere as seen in LIMS temperatures, *J. Atmos. Sci.*, 42, 557–561.
- Kamalabadi, F., J. Forbes, N. Makarov, and Y. Portnyagin (1997), Evidence for non-linear coupling of planetary waves and tides in the Antarctic mesopause, *J. Geophys. Res.*, 102, 4437–4446.
- Khattatov, B. V., et al. (1996), Dynamics of the mesosphere and lower thermosphere as seen by radars and by the high-resolution Doppler imager/UARS, *J. Geophys. Res.*, 101, 10,393–10,404.
- Kuroda, Y., and M. Chiba (1995), Creation of a zonally symmetric tide due to interference of the migrating tide and a quasi-stationary wave, *J. Meteorol. Soc. Jpn.*, 73, 737–746.
- Lieberman, R. S. (1991), Nonmigrating diurnal tides in the equatorial middle atmosphere, *J. Atmos. Sci.*, 48, 1112–1123.
- Lieberman, R. S., J. Oberheide, M. E. Hagan, E. E. Remsberg, and L. L. Gordley (2004), Variability of diurnal tides and planetary waves during November 1978–May 1979, *J. Atmos. Sol. Terr. Phys.*, 66, 517–528.
- Lieberman, R. S., J. Oberheide, and E. R. Talaat (2013), Nonmigrating diurnal tides observed in global thermospheric winds, *J. Geophys. Res. Space Physics*, 118, 7384–7397, doi:10.1002/2013JA018975.
- Livesey, N. J., et al. (2013), Earth Observing System (EOS) Microwave Limb Sounder (MLS) version 3.3 and 3.4 level 2 data quality and description document, *Tech. Rep. 81-0106*, Jet Propulsion Lab., Calif. Inst. of Technol. Pasadena, Calif.
- Manson, A. H., and C. Meek (1990), Long-period (8–10 h) wind oscillations in the upper middle atmosphere at Saskatoon (52°N): Evidence for non-linear tidal effects, *Planet. Space Sci.*, 38, 1431–1441.
- McCormack, J. P., L. Coy, and K. W. Hoppel (2009), Evolution of the quasi 2-day wave during January 2006, *J. Geophys. Res.*, 114, D20115, doi:10.1029/2009JD012239.
- McCormack, J. P., S. D. Eckermann, K. W. Hoppel, and R. A. Vincent (2010), Amplification of the quasi-two day wave through nonlinear interaction with the migrating diurnal tide, *Geophys. Res. Lett.*, 37, L16810, doi:10.1029/2010GL043906.
- Meek, C. E., and A. H. Manson (2009), Summer planetary-scale oscillations: Aura MLS temperature compared with ground-based radar wind, *Ann. Geophys.*, 27(4), 1763–1774, doi:10.5194/angeo-27-1763-2009.
- Mitchell, N. J., P. J. S. Williams, A. G. Beard, R. R. Buesnel, and H. G. Muller (1996), Non-linear planetary/tidal wave interactions in the lower thermosphere observed by meteor radar, *Ann. Geophys.*, 19, 364–366.
- Miyahara, S., Y. Miyoshi, and K. Yamashita (1999), Variations of migrating and non-migrating tides simulated by the middle atmosphere circulation model at Kyushu University, *Adv. Space. Res.*, 24, 1549–1558.
- Nielsen, K., D. E. Siskind, S. D. Eckermann, K. W. Hoppel, L. Coy, J. P. McCormack, S. Benze, C. E. Randall, and M. E. Hervig (2010), Seasonal variation of the quasi 5 day planetary wave: Causes and consequences for polar mesospheric cloud variability in 2007, *J. Geophys. Res.*, 115, D18111, doi:10.1029/2009JD012676.
- Oberheide, J., and O. A. Gusev (2002), Observation of migrating and nonmigrating diurnal tides in the equatorial lower thermosphere, *Geophys. Res. Lett.*, 29(24), 2167, doi:10.1029/2002GL016213.
- Oberheide, J., M. E. Hagan, W. E. Ward, M. Riese, and D. Offermann (2000), Modeling the diurnal tide for the CRISTA-1 time period, *J. Geophys. Res.*, 105, 24,917–24,929.
- Oberheide, J., M. E. Hagan, R. G. Roble, and D. Offermann (2002), Sources of nonmigrating tides in the tropical middle atmosphere, *J. Geophys. Res.*, 107(D21), 4567, doi:10.1029/2002JD002220.
- Oberheide, J., Q. Wu, T. L. Killeen, M. E. Hagan, and R. G. Roble (2006), Diurnal nonmigrating tides from TIMED Doppler interferometer wind data: Monthly climatologies and seasonal variations, *J. Geophys. Res.*, 111, A10S03, doi:10.1029/2005JA011491.
- Ortland, D. A., and M. J. Alexander (2006), Gravity wave influence on the global structure of the diurnal tide in the mesosphere and lower thermosphere, *J. Geophys. Res.*, 111, A10S10, doi:10.1029/2005JA011467.

- Palo, S. E., R. G. Roble, and M. E. Hagan (1999), Middle atmosphere effects of the quasi-two-day wave determined from a general circulation model, *Earth Planets Space*, **51**, 629–647.
- Pancheva, D., et al. (2002), Global-scale tidal variability during the PSMOS campaign of June–August 1999: Interaction with planetary waves, *J. Atmos. Sol. Terr. Phys.*, **64**, 1865–1896.
- Remsberg, E. E., et al. (2008), Assessment of the quality of the version 1.07 temperature-versus-pressure profiles of the middle atmosphere from TIMED/SABER, *J. Geophys. Res.*, **113**, D17101, doi:10.1029/2008JD010013.
- Sakazaki, T., K. Sato, Y. Kawatani, and S. Watanabe (2015), Three-dimensional structures of tropical nonmigrating tides in a high-vertical-resolution general circulation model, *J. Geophys. Res. Atmos.*, **120**, 1759–1775, doi:10.1002/2014JD022464.
- Schwartz, M. J., et al. (2008), Validation of the Aura Microwave Limb Sounder temperature and geopotential height measurements, *J. Geophys. Res.*, **113**, D15S11, doi:10.1029/2007JD008783.
- Siskind, D. E., M. H. Stevens, M. Hervig, F. Sassi, K. Hoppel, C. R. Englert, and A. J. Kochenash (2011), Consequences of recent Southern Hemisphere winter variability on polar mesospheric clouds, *J. Atmos. Sol. Terr. Phys.*, **73**, 2013–2021, doi:10.1016/j.jastp.2011.06.014.
- Siskind, D. E., D. P. Drob, J. T. Emmert, M. H. Stevens, P. E. Sheese, E. J. Llewellyn, M. E. Hervig, R. Niciejewski, and A. J. Kochenash (2012), Linkages between the cold summer mesopause and thermospheric zonal mean circulation, *Geophys. Res. Lett.*, **39**, L01804, doi:10.1029/2011GL050196.
- Smith, A. K., D. V. Pancheva, N. J. Mitchell, D. R. Marsh, J. M. Russell, and M. G. Mlynczak (2007), A link between variability of the semidiurnal tide and planetary waves in the opposite hemisphere, *Geophys. Res. Lett.*, **34**, L07809, doi:10.1029/2006GL028929.
- Stevens, M. H., et al. (2010), Tidally induced variations of polar mesospheric cloud altitudes and ice water content using a data assimilation system, *J. Geophys. Res.*, **115**, D18209, doi:10.1029/2009JD013225.
- Teitelbaum, H., and F. Vial (1991), On tidal variability induced by nonlinear interaction with planetary waves, *J. Geophys. Res.*, **96**, 14,169–14,178.
- Wallace, J. M., and F. R. Hartranft (1969), Diurnal wind variations, surface to 30 kilometers, *Mon. Weather Rev.*, **97**, 446–455.
- Wallace, J. M., and R. F. Tadd (1974), Some further results concerning the vertical structure of atmospheric tidal motions within the lowest 30 kilometers, *Mon. Weather Rev.*, **102**, 795–803.
- Ward, W. E., J. Oberheide, M. Riese, P. Preusse, and D. Offermann (1999), Tidal signatures in temperature data from CRISTA 1 mission, *J. Geophys. Res.*, **104**, 16,391–16,403.
- Waters, J., et al. (2006), The Earth Observing System Microwave Limb Sounder (EOS MLS) on the Aura satellite, *IEEE Trans. Geosci. Remote Sens.*, **44**(5), 1075–1092.
- Wu, Q., D. A. Orton, T. L. Killeen, R. G. Roble, M. E. Hagan, H.-L. Liu, S. C. Solomon, J. Xu, W. R. Skinner, and R. J. Niciejewski (2008a), Global distribution and interannual variations of mesospheric and lower thermospheric neutral wind diurnal tide: 1. Migrating tide, *J. Geophys. Res.*, **113**, A05308, doi:10.1029/2007JA012542.
- Wu, Q., D. A. Orton, T. L. Killeen, R. G. Roble, M. E. Hagan, H.-L. Liu, S. C. Solomon, J. Xu, W. R. Skinner, and R. J. Niciejewski (2008b), Global distribution and interannual variations of mesospheric and lower thermospheric neutral wind diurnal tide: 1. Nonmigrating tide, *J. Geophys. Res.*, **113**, A05309, doi:10.1029/2007JA012543.
- Zhang, X., J. M. Forbes, M. E. Hagan, J. M. Russell III, S. E. Palo, C. J. Mertens, and M. G. Mlynczak (2006), Monthly tidal temperatures 20–120 km from TIMED/SABER, *J. Geophys. Res.*, **111**, A10S08, doi:10.1029/2005JA011504.
- Zhu, X., J.-H. Yee, E. R. Talaat, M. Mlynczak, L. Gordley, C. Mertens, and J. M. Russell III (2005), An algorithm for extracting zonal mean and migrating tidal fields in the middle atmosphere from satellite measurements: Applications to TIMED//SABER measured temperature and tidal modeling, *J. Geophys. Res.*, **110**, D02105, doi:10.1029/2004JD004996.